

Evolution of microstructure and strength of a high entropy alloy undergoing the strain-induced martensitic transformation

Jacob Weiss ^a, Daniel J. Savage ^b, Sven C. Vogel ^b, Brandon A. McWilliams ^c, Rajiv S. Mishra ^d, Marko Knezevic ^{a,*}

^a Department of Mechanical Engineering, University of New Hampshire, Durham, NH, 03824, USA

^b Materials Science and Technology Division, Los Alamos National Laboratory, Los Alamos, NM, 87545, USA

^c Army Research Directorate, DEVCOM Army Research Laboratory, Aberdeen Proving Ground, MD, 21005, USA

^d Department of Materials Science and Engineering, University of North Texas, Denton, TX, 76207, USA



ARTICLE INFO

Keywords:

High entropy alloys
Strength
Ductility
Microstructures
Texture
Phase transformation

ABSTRACT

In a recent work, we have reported outstanding strength and work hardening exhibited by a metastable high entropy alloy (HEA), $\text{Fe}_{42}\text{Mn}_{28}\text{Co}_{10}\text{Cr}_{15}\text{Si}_5$ (in at. %), undergoing the strain-induced martensitic transformation from metastable gamma austenite (γ) to stable epsilon martensite (ε). However, the alloy exhibited poor ductility, which was attributed to the presence of the brittle sigma (σ) phase in its microstructure. The present work reports the evolution of microstructure, strength, and ductility of a similar HEA, $\text{Fe}_{38.5}\text{Mn}_{20}\text{Co}_{20}\text{Cr}_{15}\text{Si}_5\text{Cu}_{1.5}$ (in at. %), designed to suppress the formation of σ phase. A cast and then rolled plate of the alloy was processed into four conditions by annealing for 10 and 30 min at 1100 °C and by friction stir processing (FSP) at tool rotation rates of 150 and 400 revolutions per minute (RPM) to facilitate detailed examinations of variable initial grain structures. Neutron diffraction and electron microscopy were employed to characterize the microstructure and texture evolution. The initial materials had variable grain size but nearly 100% γ structure. Diffusionless strain induced $\gamma \rightarrow \varepsilon$ phase transformation took place under compression with higher rate initially and slower rate at the later stages of deformation, independent on the initial grain size. The transformation facilitated part of plastic strain accommodation and rapid strain hardening owing to a transformation-induced dynamic Hall-Petch-type barrier effect, increase in dislocation density, and texture. The peak strength of nearly 2 GPa was achieved under compression using the structure created by double pass FSP (150 RPM followed by 150 RPM). Remarkably, the tensile elongation exhibited by the alloy was nearly 20% with fracture surfaces featuring a combination of ductile dimples and cleavage.

1. Introduction

Substantial solid solution strengthening effects while avoiding brittle intermetallic phases have been achieved in a special class of materials termed high entropy alloys (HEAs) [1,2]. Several elements are usually used to produce a high configurational entropy state in these alloys for solid-solutions having extraordinary mechanical and physical properties [3]. Specifically, the alloys have shown a great potential to improve the contrasting material properties of strength and ductility [4]. HEAs began as single-phase solid solutions via equiatomic mixing of multiple elements [5] but quickly evolved into multi-elemental non-equiatomic alloy systems which undergo deformation-induced martensitic transformation [6] or precipitation strengthening [7]. Despite consisting of

multiple elements, HEAs tend to form common crystal structures for metals like face-centered cubic (FCC) or body-centered cubic (BCC). In next-generation HEAs for structural applications, single- or multi-phase solid solutions of multi-component alloy systems are sought which leverage the high entropy of mixing of constituent elements while eliminating embrittlement from secondary phases [8].

Even an equiatomic HEA, e.g. $\text{Fe}_{20}\text{Mn}_{20}\text{Ni}_{20}\text{Co}_{20}\text{Cr}_{20}$, showed outstanding strength, ductility, and fracture toughness [1]. Other variants of non-equiatomic Fe–Mn–Ni–Co–Cr HEA systems like $\text{Fe}_{40}\text{Mn}_{27.5}\text{Ni}_{26}\text{Co}_{5}\text{Cr}_2$ (at. %) or other types like $\text{Al}_{33.4}\text{Co}_{22.2}\text{Cr}_{11.1}\text{Fe}_{22.2}\text{Ni}_{11.1}$ (at. %) have been explored [6,9–12]. Modifying the composition and processing of these alloys allows tuning their microstructure and deformation characteristics [13,14]. One aspect of microstructure tuning

* Corresponding author.

E-mail address: marko.knezevic@unh.edu (M. Knezevic).

pertains to phases of multi-phase HEAs. The Fe₅₀Mn₃₀Co₁₀Cr₁₀ (at. %) alloy of the Fe–Mn–Co–Cr HEA class contains meta stable austenite (γ) with a FCC structure undergoing the strain-induced phase transformation to stable epsilon martensite (ε) persisting of a hexagonal close-packed (HCP) structure, given its low stacking fault energy (SFE) [11,15]. Volume fraction, distribution, and thermodynamic stability of γ and ε phases can be adjusted to promote ductility and strength [6,9,11,16,17]. In addition to crystallographic slip, the deformation driven transformation-induced plasticity, TRIP, mechanism accommodates plastic strain in these alloys. Depending on SFE, twinning induced plasticity (TWIP) can also operate as an additional deformation mechanism to TRIP and slip [4].

Increasing the content of Cr promotes the driving force for $\gamma \rightarrow \varepsilon$ phase transformation [18,19]. Works on the effects of adding elements such as C, Al, and Si on Fe–Mn alloys were also performed [18]. Si was found to also promote metastability of γ phase [20]. Given these findings, an HEA with chemistry of Fe₄₀Mn₂₀Co₂₀Cr₁₅Si₅ (in at. %) was developed and referred to as CS-HEA due to the increased amount of Co and added Si compared to the reference dual-phase (DP)-HEA with chemistry Fe₅₀Mn₃₀Co₁₀Cr₁₀ [9]. Increased Co and added Si stabilized and promoted ε by lowering the SFE [19,21,22]. Interestingly, the alloy exhibited both TRIP and TWIP deformation mechanisms [11,23]. In a recent work [24], we have reported outstanding strength and work hardening exhibited by a HEA with chemistry of Fe₄₂Mn₂₈Co₁₀Cr₁₅Si₅ (in at. %). However, the alloy exhibited poor ductility, which was attributed to the presence of the brittle sigma (σ) phase in its microstructure [25]. Increasing the content of V promotes the generations of sigma-phase in CoCrFeMnNiV systems [26].

Metastability of the γ phase can be further enhanced with thermo-mechanical processing which can tune stored energy, grain structure and texture in HEAs [19,21,22]. While deformation processes such as rolling or forging can change microstructure, more dramatic changes can be induced by severe plastic deformation techniques like equal channel angular pressing (ECAP), friction stir processing (FSP), and high pressure torsion (HPT) [23,27–30]. To this end, significant enhancements in strength and ductility over as-cast HEAs were obtained via FSP processing because of intense grain refinement [4,31–33]. While the as-cast Fe₄₂Mn₂₈Co₁₀Cr₁₅Si₅ (in at. %) HEA had a mixture of γ and ε with more dominance of γ phase, the FSP alloy had increased fraction of the ε phase along with substantially refined grains [20]. As a result, yield strength (YS) increased to 950 MPa relative to the 400 MPa of the as-cast counterpart. Additionally, metastability of the γ phase increases by FSP promoting $\gamma \rightarrow \varepsilon$ phase transformation because of the specific microstructure with larger stored energy.

This paper reports the microstructure and associated mechanical properties of a new DP HEA, Fe_{38.5}Mn₂₀Co₂₀Cr₁₅Si₅Cu_{1.5} (in at. %), designed to suppress the formation of σ phase in comparison to the Fe₄₂Mn₂₈Co₁₀Cr₁₅Si₅ (in at. %) composition. The addition of Cu to FeCoCrMnSi alloy systems was found to promote γ and subsequent TRIP during plastic deformation [34]. The alloy Fe_{38.5}Mn₂₀Co₂₀Cr₁₅Si₅Cu_{1.5} (in at. %) showed good fatigue resistance [35] and good corrosion resistance [34]. To complement these works and to facilitate detailed examinations of the microstructure evolution and strength under compression, the material for the present study was fabricated in four different conditions. Two of the conditions involved rolling followed by annealing for 10 and 30 min at 1100 °C to obtain two different grain sizes. The additional two conditions involved FSP using two different process parameters to obtain fine grains for enhancing strength of the alloy. One involved rolling followed by dual pass FSP under a tool rotation rate of 150 revolutions per minute (RPM) and another involved single pass FSP under a tool rotation rate of 400 RPM. The initial material in every condition was nearly single phase γ . However, different grain sizes were obtained to evaluate their role on the transformation rates and associated strength. Standard compression and tensile testing were performed to measure strength and ductility of the alloy along two testing directions. Simple compression tests were performed on

specimens to various strain levels to measure phase volume fractions and texture per phase in function of plastic strain. Neutron diffraction (NeD) and electron microscopy including electron back scatter diffraction (EBSD) were employed to characterize the phases and texture. The extent of strain induced $\gamma \rightarrow \varepsilon$ phase transformation accommodating the plasticity and texture per phase were measured and quantified for all specimens. Strength, strain hardening, and anisotropy of the alloy are rationalized and discussed in terms of the measured microstructure evolution data. Ductility in tension was also assessed.

2. Experimental procedures

2.1. Material processing

Rolled plates of Fe_{38.5}Mn₂₀Co₂₀Cr₁₅Si₅Cu_{1.5} HEA were received from Sophisticated Alloys, Inc. After vacuum arc-casting of a 50.8 mm thick ingot, the ingot was homogenized at 1100 °C for 2 h and then rolled into a half-inch thickness plate in multiple passes.

A rolled plate was processed by FSP adhering to procedures described in Refs. [4,36]. The processing was accomplished by using a W-RE tool with a shoulder diameter of 16 mm and a root diameter of 8 mm. The shoulder contained a tapered pin with a diameter of 6 mm and a length of 4 mm. Two FSP beads were created in the rolled plate using two rotational rates. The 1st FSP bead was a two-pass bead made with a rotational tool rate of 150 RPM for both passes with a length of 107 mm. The 2nd FSP bead had a 400 RPM tool rotation rate with again a length of 107 mm. The traverse speed was 50.8 mm/min for both rotational rates. FSP was completed along the rolled plate's transverse direction (TD). Samples for compression testing were machined from the two FSP beads and classified into two categories: 150 RPM dual-pass FSP and 400 RPM single pass FSP as “S1” and “S2”, respectively. The diameter and height of the compression cylinders were within the FSP beads.

Two additional plates of the initial rolled HEA were subjected to heat treatment only. Annealing at 1100 °C for 30 min for the first plate and annealing at 1100 °C for 10 min for the second plate were performed. Samples for compression testing were machined from these two plates as well. Two additional specimen categories are: as-rolled + annealed at 1100 °C for 30 min and as-rolled + annealed at 1100 °C for 10 min and denoted as “S3” and “S4”, respectively.

2.2. Mechanical testing

Wire electrical discharge machining (EDM) was used to machine the cylinders for compression testing from the plates along two directions to evaluate any possible anisotropy: the in-plane (IP) TD and the through thickness (TT) normal direction (ND). The remaining plate direction is the rolling direction (RD). Cylinders of 4 mm diameter and 4 mm height were made from the four categories. Test results for S3 and S4 specimens were verified using cylinders of 6 mm in diameter and 8 mm in height. Tensile samples were machined using EDM and turned from the S3 category along the RD. The gauge section of the dog-bone tensile specimens was 25 mm in length and 5 mm in diameter.

An Instron servo-hydraulic testing machine with appropriate fixtures was used for the compression and tensile tests. All tests were conducted at room temperature and at a constant quasi-static strain rate of 10^{-3} /s. The load cell used had a capacity of 100 kN. The machine was controlled using an integrated DAX software. Lubricant oil was used to reduce friction between the sample and the die. A steel ball was placed between the upper force arm and the upper platen to eliminate bending moment and to ensure a uniaxial state. Compliance of the machine was measured and subtracted from the raw compression data to correct the load and displacement data before the true-stress true-strain curves were calculated [37,38]. Tests were performed to specific strain levels or to fracture to investigate microstructure evolution at these strains. Tensile tests were also repeated and no appreciable difference between the measured curves was detected.

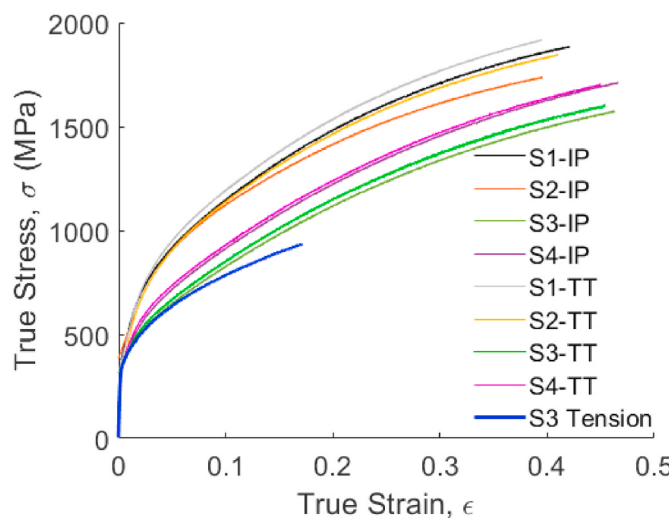


Fig. 1. True stress versus true strain curves for the four specimen categories compressed to fracture in both in-plane (IP)/TD and through thickness (TT)/ND directions and for one specimen category pulled to fracture in tension along RD.

2.3. Microstructural characterization

2.3.1. Electron microscopy

Microstructure in the specimens was characterized by EBSD, energy dispersive spectroscopy (EDS), and secondary electrons (SE) imaging in a scanning electron microscope (SEM). These were performed using a Tescan Lyra (Ga) field emission SEM. EBSD scans were taken in field mode with a beam intensity (BI) of 20.05–20.07 at a voltage of 20 kV. The working distance was set at 9 mm and the scans were conducted with a step size of 0.2 μm at 10×10 binning for S1 and S2 categories and with a step size of 0.3 μm at a 16×16 bin size for S3 and S4 categories. Multiple scans were taken for each strain level to ensure sufficient statistics of the results and all scans contained over 600,000 points. Post processing of data was performed using orientation imaging microscopy (OIM) analysis software package.

Samples cross sections from specimens were prepared by grinding with 320, 400, and 800 grit SiC papers with 6lb force per sample till plane. Post grinding, the samples were polished with a TriDent mat using 3 μm diamond suspension at 150 rpm for 5 min, followed by a TriDent mat with 1 μm diamond suspension at 150 rpm for 5 min. Lastly, vibratory polishing with a 0.04 μm colloidal silica suspension for 28 h was conducted to ensure preferable indexing and high confidence index (CI) on the EBSD scans. Vibratory polishing was necessary to ensure no $\gamma \rightarrow \epsilon$ transformation was induced by the polishing process.

EDS was also completed at 15 kV voltage and 9 mm working distance to confirm the elemental composition.

Finally, several SE images of fractured surfaces were captured.

2.3.2. Neutron diffraction

Neutron diffraction (NeD) was conducted at Los Alamos Neutron Science Center (LANSCE) at Los Alamos National Laboratory. The time-of-flight (TOF) high pressure preferred orientation (HIPPO) neutron diffractometer was used to obtain diffraction data for quantitative phase and texture analyses. HIPPO detector rings are normally positioned at 20 diffraction angles of 40°, 60°, 90°, 120°, and 144°. In the instrument, sample cylinders were oriented with the loading direction (LD) perpendicular to the neutron beam. To improve pole figure coverage, three sample rotations (0°, 67.5°, and 90°) around LD were used, resulting in a total of 126 unique diffraction vectors after noisy detectors were removed. For phase identification, the diffraction data for each ring and the three rotations was summed, resulting in 5 histograms. The summed data ensures the phase analysis is mostly free from texture in-

fluence; simplifying identification of minority phases [24]. Rietveld analysis was performed with MAUD [39–41] using the scripting analysis software MILK [42]. The 10° E-WIMV textures were exported from MAUD for plotting and analysis in MTEX [43].

3. Results

3.1. Mechanical testing

True stress-strain curves were measured under compression testing of the four alloy conditions. Additionally, a true stress-strain curve of S3 condition was measured in tension. The data is presented in Fig. 1. As apparent from the figure, the S3 condition material category has the lowest strength. The as-rolled + annealed alloy is relatively isotropic and can accumulate slightly more compressive strain in IP than TT. Strength of the material increased with FSP as seen from the curves of S1 and S2 specimens. The different tooling rates created slightly varying microstructures, as described in the following sections. Decreasing the tool speed from 400 RPM to 150 RPM double pass increased the strength of the alloy. The S1 category material tested along the TT direction showed the highest strength of over 1900 MPa. The increase in strength from S3 to S4 did not result in loss of compressive strain at fracture. The FSP materials showed slightly more anisotropy than the rolled + annealed plates. Directional dependence of compressive strength did not have a large variance in TT and IP directions. However, for all material categories, the TT direction displayed slightly higher strength than the IP direction.

Simple tension was conducted for the as-rolled S3 material category because of sufficient material to make tensile specimens. Multiple samples were tested. The material displayed good strain accommodation fracturing at 0.18 strain level. This is substantially larger than a previously tested FeMnNiCoCrSi system due to the elimination of a brittle sigma phase [25] (Appendix A). To further understand the strength behavior of the four material conditions, EBSD and NeD characterizations were performed and presented below.

3.2. Microstructural evolution

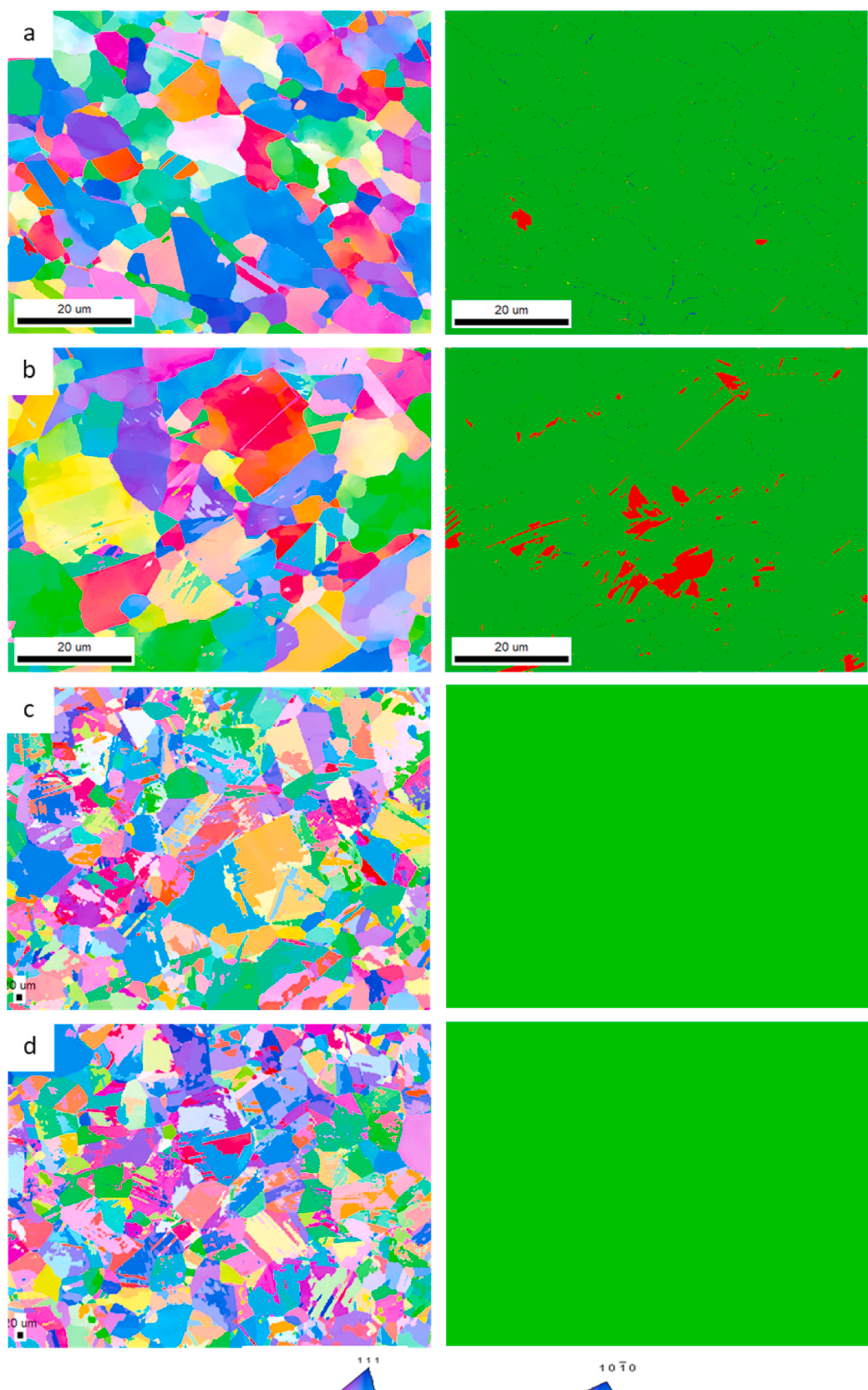
3.2.1. EBSD

Inverse pole figure (IPF) maps and phase maps of the initial structures are shown in Fig. 2. The two phases are shown with green and red colors, which correspond to γ -austenite and ϵ -martensite, respectively. Evidently, the initial materials contain very little ϵ . Note that both tool rotation rates (150 RPM and 400 RPM) take the material into the γ phase to sufficiently soften the material for FSP. The structure does not contain any σ like the HEA studied in our prior work [24]. Average grain size of γ phase was estimated for every material category and is provided in Table 1. FSP processing at higher tooling rates put a higher heat into the material to facilitate slightly more grain growth.

Figs. 3 and 4 shows the microstructure and phase maps of the four material categories at a compressive strain of approximately 0.1 and 0.3, respectively. Slip bands of γ phase as sheaves of parallel laths on the {111} γ planes produce the strain induced ϵ formation while being able to accommodate the plastic strain. The deformed structures at 0.3 strain contain a small fraction of deformation twins.

3.2.2. Neutron diffraction

Example summed patterns from the 90° HIPPO detectors is presented in Fig. 5 for S4-IP specimen. A Rietveld model fit (red) without texture demonstrates that the summing procedure effectively removed any texture and allows visual identification of phase fraction evolution. Data for all other specimens look similar. Bragg reflections for the two present phases are shown in the figure. Evidently, the intensity of γ phase decreases with increasing compressive strain, while the intensity of ϵ increases. In the absence of texture, this intensity change is indicative of the phase fractions evolving with strain.



(caption on next page)

Fig. 2. IPF and corresponding phase maps acquired by EBSD for the initial specimens: (a) S1-IP, (b) S2-IP, (c) S3-IP, and (d) S4-IP. Perpendicular to the maps is the sample IP/TD direction. The colors in the IPF maps also represent the orientation of TD/IP sample axis with respect to the crystal frame according to the coloring in the standard IPF triangles shown at bottom. Phase fraction values are averages of at least two scans: 98% FCC in (a), 94% FCC in (b) and 100% FCC in (c) and (d). The micron bars in the maps are 20 μm . (For interpretation of the references to color in this figure legend, the reader is referred to the Web version of this article.)

Table 1
Average grain size in the γ phase of initial specimens.

Category	FCC (μm)	Standard deviation (μm)
S1	8	4.1
S2	16	5.2
S3	90	32.5
S4	70	22.5

The results of the phase analysis are presented in Fig. 6. The figure also includes the EBSD data. There is an obvious change in the phase fractions due to the strain induced transformation process. The trends are such that the transformation is more rapid initially and slows down at higher strain levels. The saturation is at about 20% of remaining γ . Local EBSD measurements shows a slightly higher rate of transformation, but NeD data are macroscopic and more representative. Interestingly, all sample categories show the similar transformation rate.

Pole figures showing the texture evolution for both γ and ϵ phases are presented in Fig. 7. Refinements of 132 histograms from the NeD data was used to reconstruct an ODF per specimen per phase. Analysis was performed using E-WMIV texture algorithm and followed the processes described in Ref. [44]. Evidently, the initial texture of all sample categories for both γ and ϵ were relatively random. As anticipated, the pole figures for γ phase exhibit strengthening of the $\{110\}$ fiber along the loading direction with compressive strain for all sample categories [44–46]. ϵ phase strengthens basal pole, $\{0001\}$, along the loading direction because of $\gamma \rightarrow \epsilon$ phase transformation. Such texture can promote pyramidal slip and twinning [47].

4. Discussion

Results have shown that the alloy exhibits a good synergy of strength, work hardening, and ductility owing primarily to the great deal of $\gamma \rightarrow \epsilon$ martensitic transformation. The 1.5 at. % Cu in the alloy stabilized the metastable γ independent on the thermomechanical processing explored in the present work [34]. The phases in the four material categories were determined by NeD. Moreover, the EBSD maps were collected to partially cross validate the macroscopic NeD data and to confirm occurrence of deformation twins in the structure. The IPF maps also depicted the process of slip bands as sheaves of parallel laths stringing out on the $\{111\}_\gamma$ planes in the γ phase forming the strain-induced ϵ , while accommodating plastic strain.

The studied HEA exhibited an extensive diffusionless transformation of metastable γ into stable ϵ under compression. The ϵ phase was stable in the FeMnCoCr HEA system at room temperature. The driving force or the change in Gibb's free energy for $\gamma \rightarrow \epsilon$ transformation was primarily related to the change in entropy [48]. The metastability of γ was increased in the alloy by adding the ϵ phase stabilizers, Co and Si, which increased the entropy and lowered the SFE of the alloy. The low SFE was necessary for the formation of ϵ . Local stress field acting in individual grains could separate partial dislocations into slip bands [49,50]. Such bands encompassed nearby $\{111\}_\gamma$ planes and formed thick faults [51]. Dislocations at every 2nd $\{111\}_\gamma$ plane in a γ band formed ϵ HCP structure [52]. In contrast, dislocations at every $\{111\}_\gamma$ plane in a γ band would form FCC twin structure.

In general, whether ϵ or twin forms in a γ band depends on the SFE [48]. Stress for the dissociation of perfect dislocations into partials to form stable intrinsic stacking faults in the γ matrix decreases with decreasing SFE. Crystallographically soft grains have a higher tendency to transform [53–58]. To this end, grains with the $\langle 001 \rangle$

crystallographic direction parallel to the compression direction easily transform forming slip bands of ϵ [56], while the orientations compressed along $\langle 111 \rangle$ or $\langle 011 \rangle$ directions cannot transform in compression because partial dislocations do not have sufficient driving force to produce wide stacking faults and slip bands [54,57]. Fig. 7 shows relatively weak initial texture in the studied materials meaning that texture plays a secondary role in the transformation kinetics (e.g. comparing transformation behavior of TD and ND compression). Stored energy and defect contents in the structure also influence the transformation kinetics.

The tool rotation rate of 400 RPM during FSP developed a higher temperature than the 150 RPM rate. Both rates took the material into the soft γ phase. During any FSP, grains substantially refined while some recovery, dynamic recrystallization, and grain growth took place [31]. The lower tool rotation rate developing lower temperature left a higher stored energy in the structure than the higher tool rotation rate developing a higher temperature. The higher stored energy state means a higher dislocation density content in the structure. The high stored energy state of the structure corresponds to the high enthalpy state, even though the entropy is the same because the solid solution configurations remain the same [59]. While the fraction of phases during compression was not found to be a strong function of the processing history or compression direction, measured results in Fig. 6 show slightly more of the ϵ phase upon FSP at 150 RPM than upon FSP at 400 RPM meaning that the structure in the former condition promoted the transformation slightly more than in the latter condition. Strain hardening rates are influenced by the rate and amount of the ϵ phase. For example, the rate and amount of transformation in S2-IP specimen is slightly less than in S1-IP, S1-TT, and S2-TT and therefore the rate of hardening is correspondingly slightly smaller. Likewise, the less annealed material S4 having a bit higher stored energy transformed a bit more than the more annealed material S3 (Fig. 6). Finally, the data shows a slightly greater $\gamma \rightarrow \epsilon$ transformation rate in the TT direction than in the IP direction.

The phases in the structure are co-deforming contributing to texture evolution per phase (Fig. 7). Deformation initiates from slip in the γ phase, and subsequently progresses into the ϵ martensitic transformation. The deformation in ϵ proceeds on prismatic and basal planes, which later progresses through non-basal slip activity and some deformation twinning [60]. The non-basal slip activity is promoted with texture evolution as crystallographic c-axis for many grains becomes aligned or slightly tilted with respect to the compression direction. Texture evolution in γ during compression forms a typical $\{110\}$ fiber owing to the crystallographic slip on octahedral slip systems [61–63]. Texture evolution in ϵ is primarily driven by the variant selection during transformation. The crystallographic relationship between γ and ϵ is $\{111\}_\gamma \parallel \{0001\}_\epsilon, \langle 110 \rangle_\gamma \parallel \langle 21\bar{1}0 \rangle_\epsilon$ [44]. Moreover, the ϵ phase deforms by multiple slip modes and some twinning, all contributing to the texture evolution. As a result, there is some texture induced hardening, especially in the ϵ phase, for all material categories.

The behavior of the alloy under compression featured a great deal of plasticity and strain hardening before fracture. The fraction of ϵ increased at the expanse of γ due to the diffusionless strain induced $\gamma \rightarrow \epsilon$ phase transformation, as explained above. The evolution of phases and texture data was used to rationalize the overall hardening of the HEA studied in the present work. 150 RPM FSP S1 material was the strongest because of the smallest initial grain size and the highest dislocation density to begin with, while the 30 min annealed material S3 was the softest because of the coarsest grain size and likely the smallest density of dislocations. All four material categories underwent substantial microstructural changes under compression with similar transformation

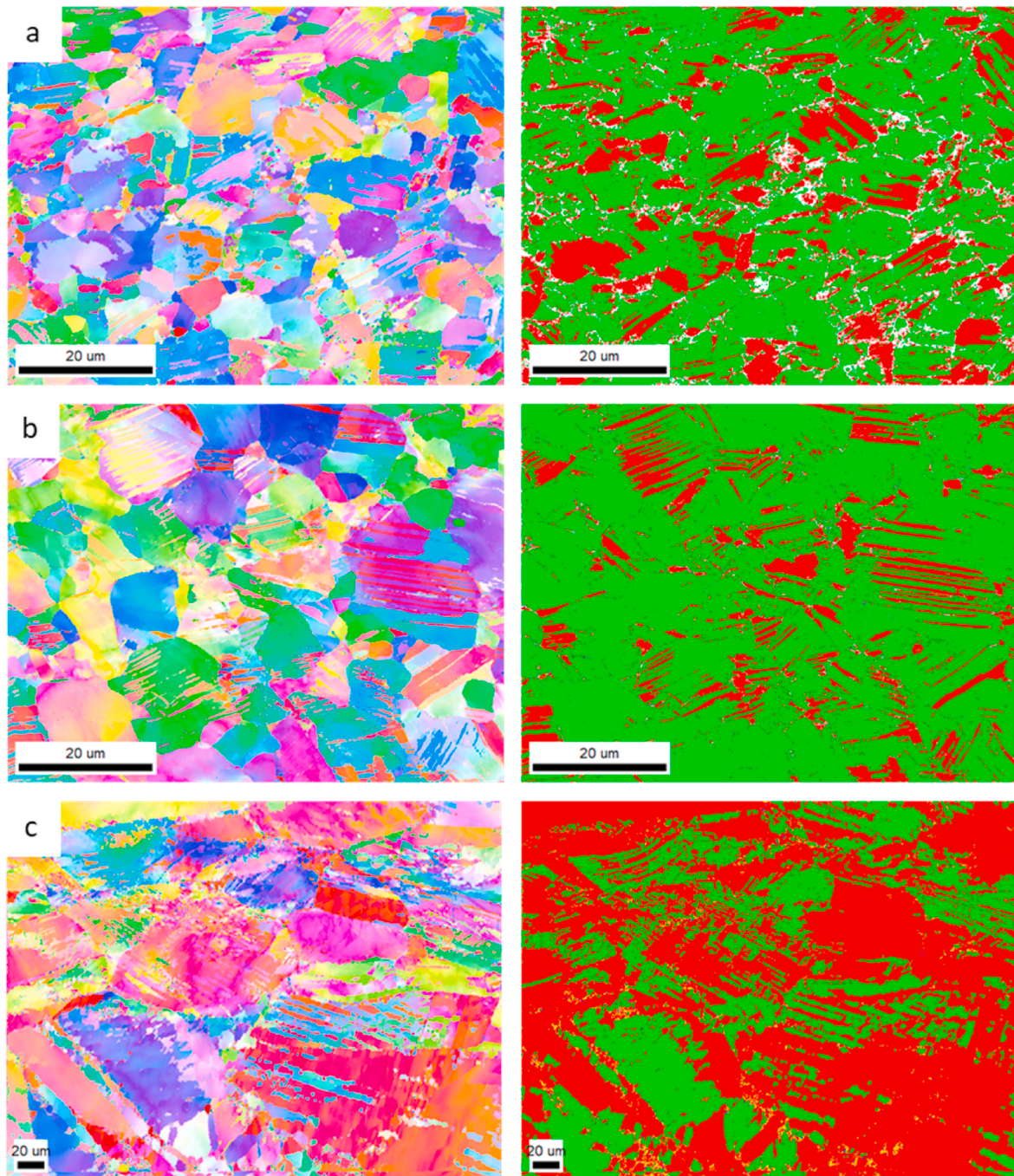


Fig. 3. IPF and corresponding phase maps acquired by EBSD for specimens compressed to approximately $\varepsilon = 0.1$: (a) S1-IP, (b) S2-IP, and (c) S3-IP. The colors in the IPF maps are defined as in Fig. 2. Phase fraction values are averages of at least two scans: 66% FCC in (a), 70% FCC in (b) and 37% FCC in (c). The micron bars in the maps are 20 μm . (For interpretation of the references to color in this figure legend, the reader is referred to the Web version of this article.)

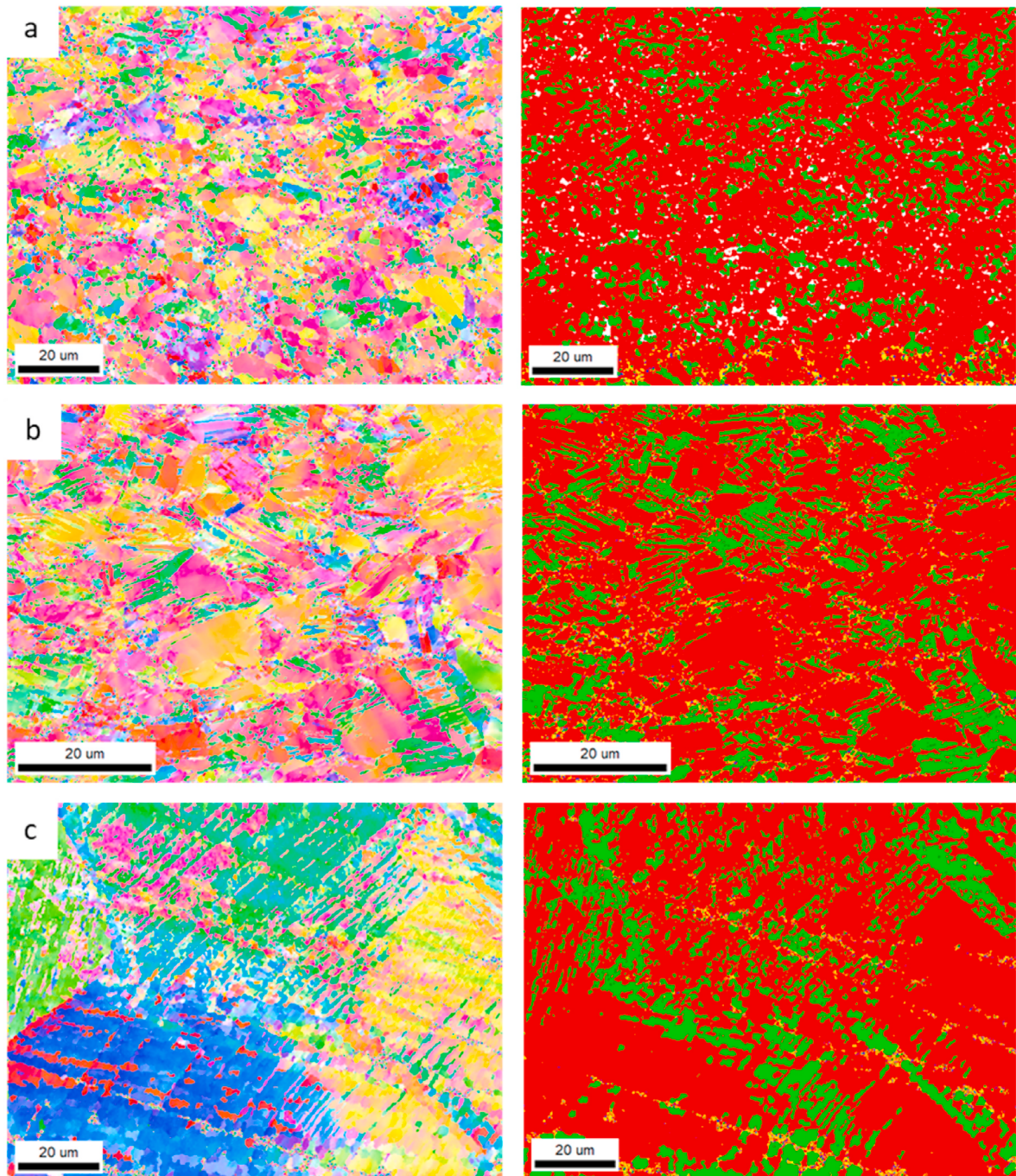


Fig. 4. IPF and corresponding phase maps acquired by EBSD for specimens compressed to approximately $\varepsilon = 0.3$: (a) S1-IP, (b) S2-IP, and (c) S3-IP. The colors in the IPF maps are defined as in Fig. 2. Phase fraction values are averages of at least two scans: 18% FCC in (a), 26% FCC in (b) and 28% FCC in (c). The micron bars in the maps are 20 μm . (For interpretation of the references to color in this figure legend, the reader is referred to the Web version of this article.)

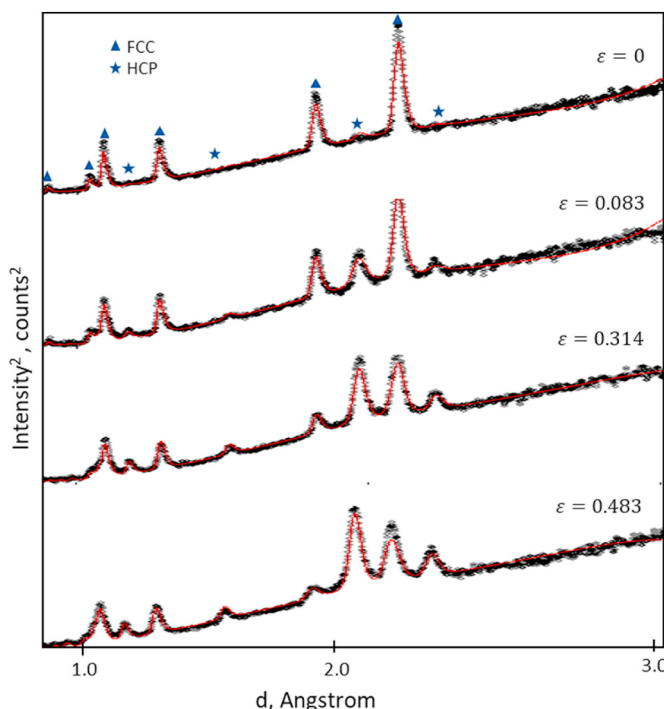


Fig. 5. Measured diffraction patterns (black) along with Rietveld refinement fits (red) for S4-IP specimen at the four strain levels indicated in the figure. The y-axis is the square-root of the intensity of peaks in the square root of counts of photons, while the x-axis is a selected range of the interplanar spacing. (For interpretation of the references to color in this figure legend, the reader is referred to the Web version of this article.)

rates governing similar hardening rates. The material S1 is the strongest and exhibited the most rapid hardening because of the smallest initial grain size complemented with the dynamic Dynamic Hall-Petch (HP)-type barrier effect due to the transformation. The dynamic HP hardening originated from interfaces in the microstructure forming barriers to mobile dislocations as the transformation progresses. The HP effect was found to be very effective in hardening the material categories with more for the smaller grain size structures. Given a slightly higher $\gamma \rightarrow \epsilon$ transformation rate along TT than IP, the TT curves were slightly stronger than the IP curves for all material categories.

Microstructural defects introduced by prior thermos-mechanical processing are necessary for the strain-induced structural transformation process to begin. The transformation begins by the formation of slip bands. The bands occur and grow as partial dislocations separate under the action of local stress fields. While defect content is important for the onset, the local stress fields in suitably oriented grains are important for growth of the ϵ phase. While grain boundaries act as nucleation sites for ϵ , fine grain structures induce heterogeneous stress fields varying from grain to grain. Such stress fields hinder the transformation process. Moreover, back-stress fields and higher stability of grain boundaries can hinder the growth of ϵ [64–66]. The insignificant role of grain size on the TRIP behavior of the studied materials is a compromised effect of the listed phenomena balancing nucleation and propagation. The smaller grained materials have more defects and stored energy owing to the FSP processing and have more grain boundaries to provide more nucleation sites promoting the transformation, but the large content of grain boundaries and heterogeneous stress fields hinder the transformation growth. In contrast, the coarser grained materials have less defects to begin the transformation, but the growth is easier.

In closing, we present fractography of a broken tensile S3 specimen. A combination of ductile fracture with dimpled morphology and some areas showing more brittle inter-granular characteristics was observed (Fig. 8). The smooth flat surfaces over multiple grains are evidence of cleavage. Enlarged views of the fracture surface with dimples show lack of stretching i.e. void growth implying the incapability of the alloy to accommodate plastic flow upon exhausting the uniform elongation. The alloy fractures right after reaching ultimate tensile strength with a complete lack of non-uniform deformation in tension. The lack of non-uniform deformation is a consequence of the TRIP in part because of tensile residual stress fields resulting from the FCC-to-HCP structural change inducing volume contraction. Cracks open and rapidly propagate through such fields.

5. Conclusions

In this study, strength, hardening, ductility, and microstructure evolution of a very low SFE $\text{Fe}_{38.5}\text{Mn}_{20}\text{Co}_{20}\text{Cr}_{15}\text{Si}_5\text{Cu}_{1.5}$ (in at. %) HEA were investigated. The primary focus of the work was on the structure evolution during compression beginning from the variable initial microstructures of the alloy created by annealing and FSP. The initial microstructures contained metastable γ promoted by the alloy composition including Cu. The alloy showed tremendous microstructural flexibility by controlling the extent of the transformation from $\sim 0\%$ to $\sim 80\%$ of ϵ content. Hardening was a direct consequence of the extent of the transformation inducing the structural refinement and underlying dynamic HP barrier effect. The main conclusions are.

- A great deal of hardening of the alloy under compression could result with strength of nearly 2 GPa. The peak strength was attained by the FSP material undergoing the dynamic structure refinement by transformation under compression. Dual pass FSP at 150 RPM refined grains more than FSP at 400 RPM because the 400 RPM FSP developed higher temperature fields promoting recovery and recrystallization more than 150 RPM FSP. Therefore, the 150 RPM FSP material exhibited the most rapid hardening because of the smallest initial grain size complemented with the dynamic HP effect due to the transformation.
- While the fraction of phases during compression was not found to be a strong function of the processing history or compression direction, measured results revealed slightly more of the ϵ phase upon FSP at 150 RPM than upon FSP at 400 RPM meaning that the structure in the former condition promoted the transformation slightly more than in the latter condition. Likewise, the less annealed material having a bit higher stored energy transformed a bit more than the more annealed material.
- Measuring the rate of austenite to martensite transformation during compression in function of the initial grain size revealed only a secondary dependence. Moreover, the transformation took place under compression with a high rate initially and a slower rate at the later stages of deformation independent on the initial grain size. The transformation was exhausted at approximately 20% of retained γ .
- Texture of the γ phase after compression was a {110} fiber, while texture of the ϵ phase was basal relative to the compression direction owing to the reorientation during transformation. As a result of the basal texture in ϵ , non-basal slip systems must have activated to accommodate portion of the compressive strains contributing to some texture hardening of the alloy.
- Tensile elongation exhibited by the alloy in its annealed condition was found to be nearly 20% with fracture surfaces featuring a combination of ductile dimples and cleavage. The successful elimination of the σ phase allowed for substantially increased ductility of the

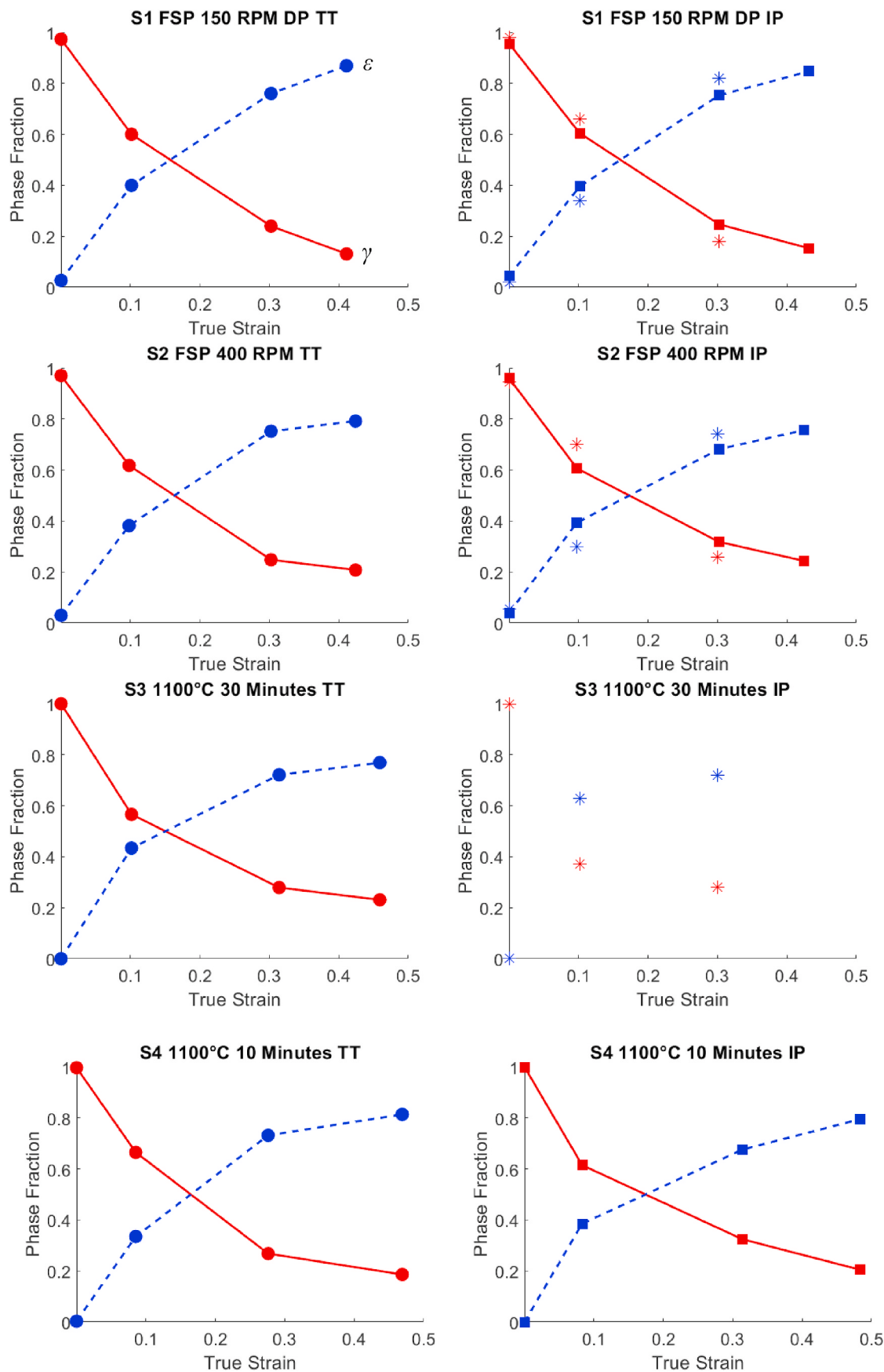


Fig. 6. Evolution of phase fractions (FCC-red, HCP-blue) with plastic strain under compression along TT (left) and IP (right) for specimens of the HEA labeled in the figure. Circular and square symbols are data measured by NeD, while stars are data collected using EBSD. Lines are fit to show the transformation rate trends. The actual rates are presented in the appendix. (For interpretation of the references to color in this figure legend, the reader is referred to the Web version of this article.)

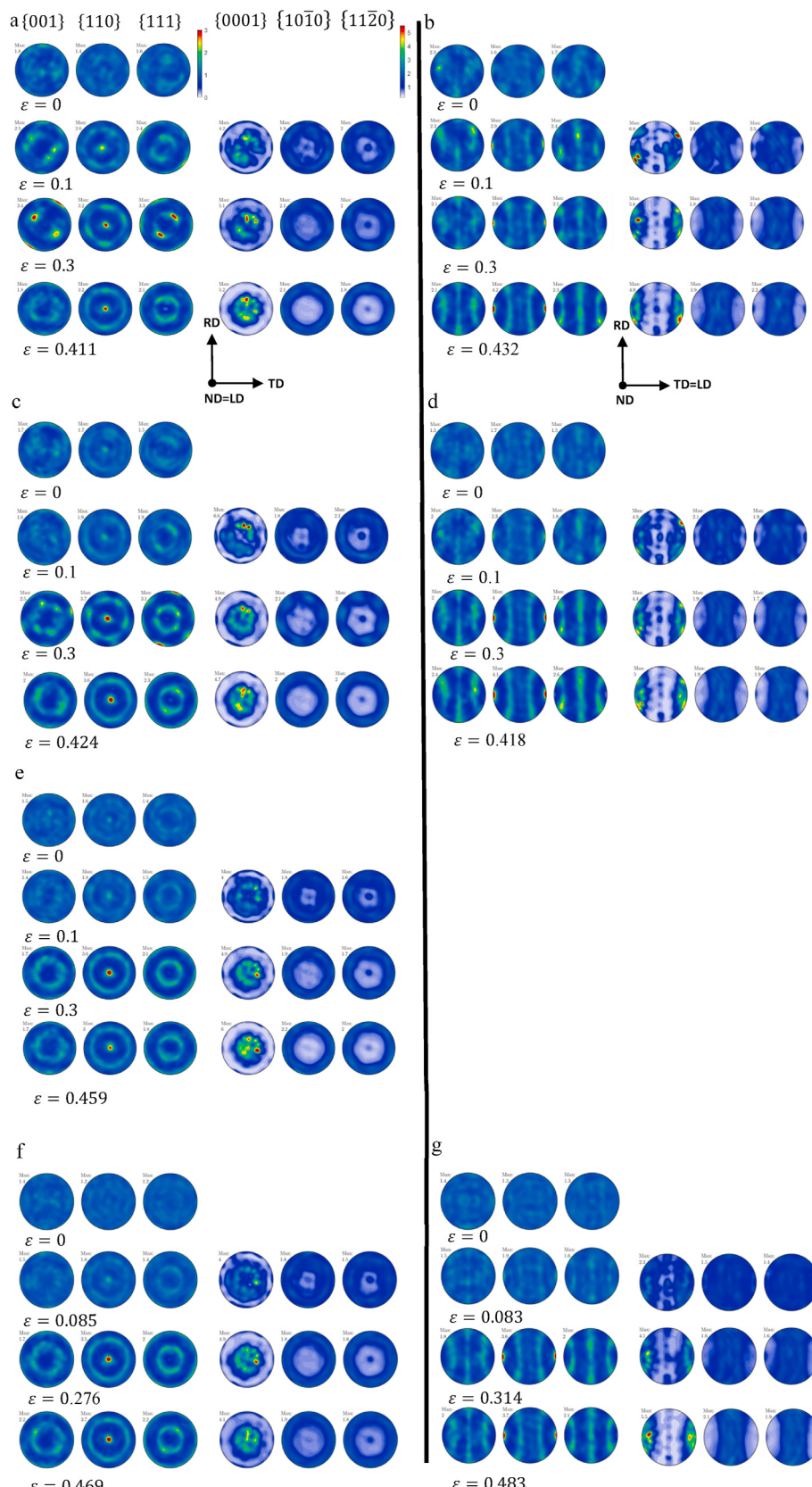


Fig. 7. Stereographic pole figures measured using NeD showing the evolution of texture in FCC austenite and HCP martensite phases during compression at the indicated strain levels for: (a) S1-TT, (b) S1-IP, (c) S2-TT, (d) S2-IP, (e) S3-TT, (f) S4-TT, and (g) S4-IP sample categories. Loading direction (LD) is indicated in the figure.

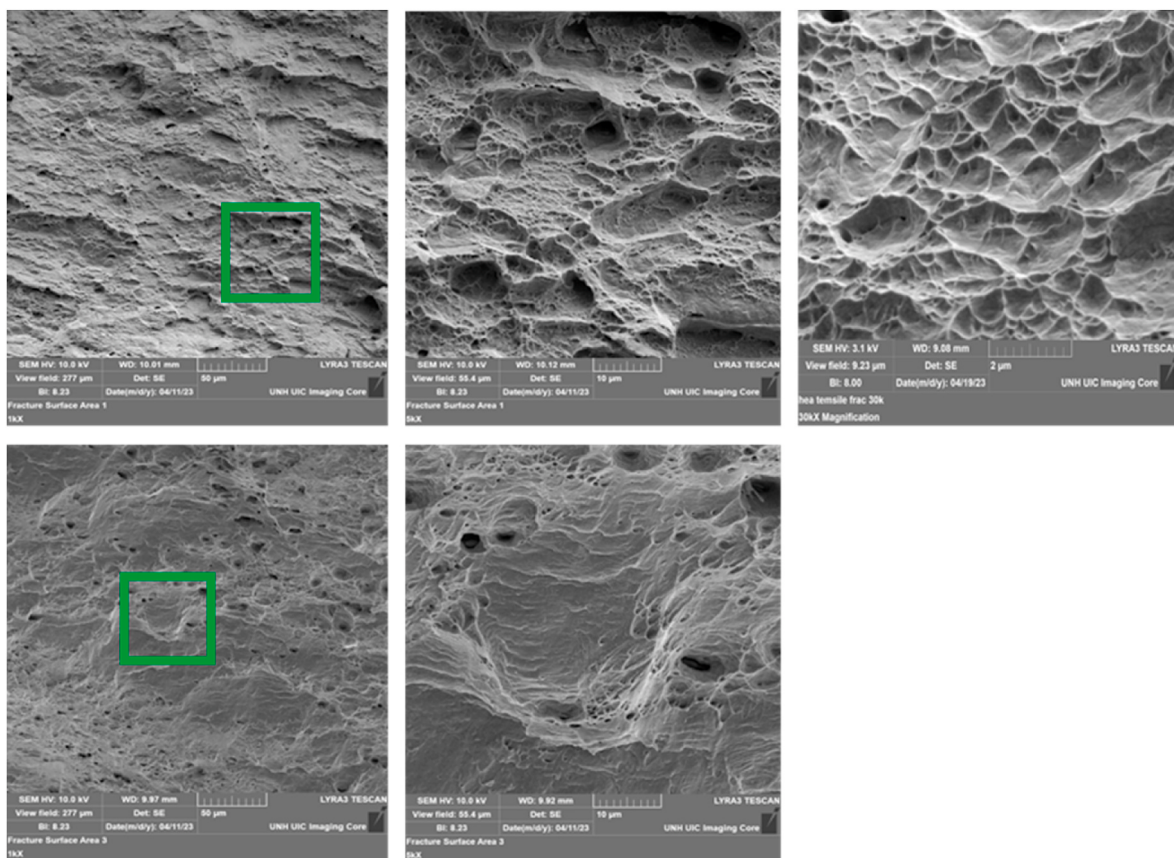


Fig. 8. Fractography images showing the fracture surface features of an S3 specimen pulled to fracture in tension: dimpled morphology in the upper row and smooth flat surfaces in the bottom row.

alloy relative to the previously studied alloy, Fe₄₂Mn₂₈Co₁₀Cr₁₅Si₅ (in at. %), containing σ.

CRediT authorship contribution statement

Jacob Weiss: Validation, Formal analysis, Investigation, Data curation, Writing – original draft, Visualization. **Daniel J. Savage:** Methodology, Software, Formal analysis. **Sven C. Vogel:** Methodology, Software, Formal analysis. **Brandon A. McWilliams:** Investigation, Resources, Project administration. **Rajiv S. Mishra:** Conceptualization, Investigation, Writing – review & editing, Supervision. **Marko Knezevic:** Conceptualization, Methodology, Investigation, Resources, Writing – review & editing, Supervision, Project administration, Funding acquisition.

Declaration of competing interest

The authors declare that they have no known competing financial

interests or personal relationships that could have appeared to influence the work reported in this paper.

Data availability

Data will be made available on request.

Acknowledgements

This research was supported by the DEVCOM Army Research Laboratory under cooperative agreement no. W911NF-21-2-0149 and the U. S. National Science Foundation under grant no. OIA-1757371. SCV and DJS gratefully acknowledge funding by the U.S. Department of Energy (DOE) through the Los Alamos National Laboratory. Los Alamos National Laboratory is operated by Triad LLC, for the National Nuclear Security Administration of the U.S. DOE under Contract No. 89233218CNA000001.

Appendix A

Fig. 1A shows compressive and tensile strength of an as-rolled quadruplex HEA Fe₄₂Mn₂₈Co₁₀Cr₁₅Si₅ (in at. %) [25]. **Fig. A2** shows the transformation rates.

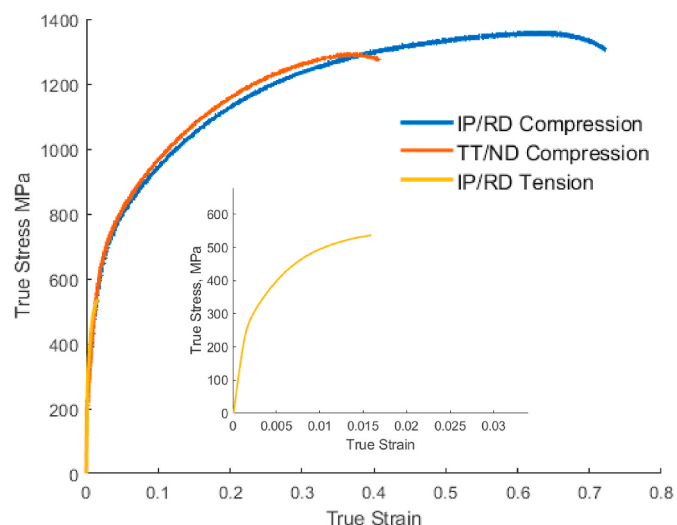


Fig. A1. True stress versus true strain curves for the specimens of Fe₄₂Mn₂₈Co₁₀Cr₁₅Si₅ (in at. %) HEA tested along IP and TT directions in compression and along IP direction in tension to fracture. The plot of the tensile curve is zoomed in for clarity.

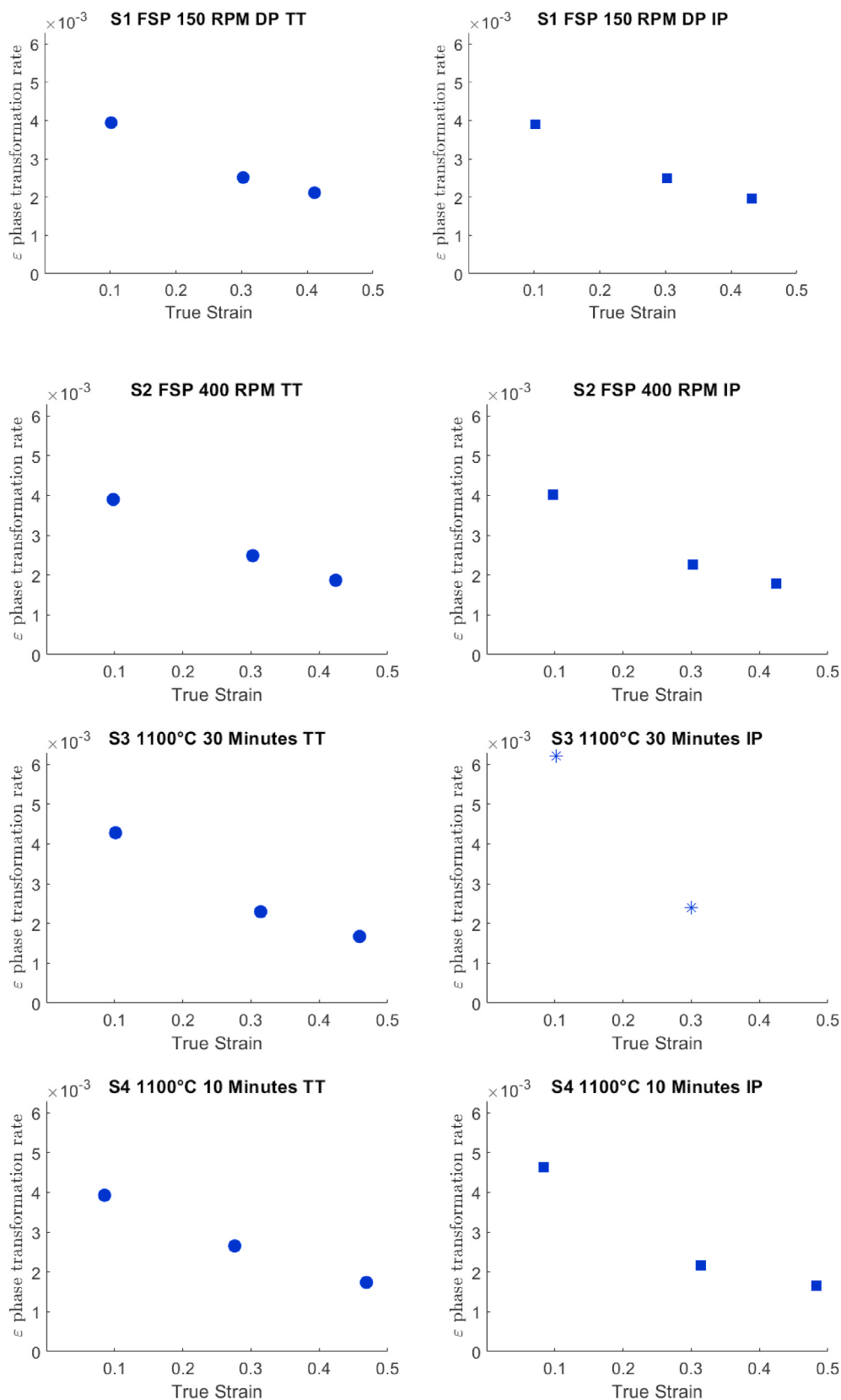


Fig. A2. Evolution of transformation rates vs. true strain for ε phase under compression along TT (left) and IP (right) for specimens of the HEA labeled in the figure.

References

- [1] B. Cantor, Multicomponent and high entropy alloys, *Entropy* 16 (2014) 4749–4768.
- [2] J.W. Yeh, S.K. Chen, S.J. Lin, J.Y. Gan, T.S. Chin, T.T. Shun, C.H. Tsau, S.Y. Chang, Nanostructured high-entropy alloys with multiple principal elements: novel alloy design concepts and outcomes, *Adv. Eng. Mater.* 6 (2004) 299–303.
- [3] R.S. Haridas, A. Gumaste, P. Agrawal, S. Yadav, R.S. Mishra, Favorable property integration in high entropy alloys via dissimilar friction stir welding: a case study using Al0.3CoCrFeNi and Fe38.5Co20Mn20Cr15Si5Cu1.5 HEAs, *Mater. Today Commun.* 35 (2023), 105822.
- [4] S.S. Nene, M. Frank, K. Liu, S. Sinha, R.S. Mishra, B. McWilliams, K.C. Cho, Reversed strength-ductility relationship in microstructurally flexible high entropy alloy, *Scripta Mater.* 154 (2018) 163–167.
- [5] B. Cantor, I.T.H. Chang, P. Knight, A.J.B. Vincent, Microstructural development in equiatomic multicomponent alloys, *Mater. Sci. Eng.* 375–377 (2004) 213–218.
- [6] Z. Li, K.G. Pradeep, Y. Deng, D. Raabe, C.C. Tasan, Metastable high-entropy dual-phase alloys overcome the strength-ductility trade-off, *Nature* 534 (2016) 227–230.
- [7] J.Y. He, H. Wang, H.L. Huang, X.D. Xu, M.W. Chen, Y. Wu, X.J. Liu, T.G. Nieh, K. An, Z.P. Lu, A precipitation-hardened high-entropy alloy with outstanding tensile properties, *Acta Mater.* 102 (2016) 187–196.
- [8] J.-W. Yeh, S.-K. Chen, S.-J. Lin, J.-Y. Gan, T.-S. Chin, T.-T. Shun, C.-H. Tsau, S.-Y. Chang, Nanostructured high-entropy alloys with multiple principal elements: novel alloy design concepts and outcomes, *Adv. Eng. Mater.* 6 (2004) 299–303.
- [9] Z. Li, C.C. Tasan, K.G. Pradeep, D. Raabe, A TRIP-assisted dual-phase high-entropy alloy: grain size and phase fraction effects on deformation behavior, *Acta Mater.* 131 (2017) 323–335.
- [10] Y. Deng, C.C. Tasan, K.G. Pradeep, H. Springer, A. Kostka, D. Raabe, Design of a twinning-induced plasticity high entropy alloy, *Acta Mater.* 94 (2015) 124–133.
- [11] Z. Li, D. Raabe, Strong and ductile non-equiatomic high-entropy alloys: design, processing, microstructure, and mechanical properties, *Jom* 69 (2017) 2099–2106.
- [12] M.J. Yao, K.G. Pradeep, C.C. Tasan, D. Raabe, A novel, single phase, non-equiatomic FeMnNiCoCr high-entropy alloy with exceptional phase stability and tensile ductility, *Scripta Mater.* 72–73 (2014) 5–8.
- [13] A.M. Manzoni, U. Glatzel, New multiphase compositionally complex alloys driven by the high entropy alloy approach, *Mater. Char.* 147 (2019) 512–532.
- [14] G.A. Salishchev, M.A. Tikhonovsky, D.G. Shaysultanov, N.D. Stepanov, A. V. Kuznetsov, I.V. Kolodiy, A.S. Tortika, O.N. Senkov, Effect of Mn and V on structure and mechanical properties of high-entropy alloys based on CoCrFeNi system, *J. Alloys Compd.* 591 (2014) 11–21.
- [15] B. He, B. Hu, H. Yen, G. Cheng, Z. Wang, H. Luo, M. Huang, High dislocation density-induced large ductility in deformed and partitioned steels, *Science* 357 (2017) 1029–1032.
- [16] Z. Feng, E.M. Mamros, J. Ha, B.L. Kinsey, M. Knezevic, Modeling of plasticity-induced martensitic transformation to achieve hierarchical, heterogeneous, and tailored microstructures in stainless steels, *CIRP Journal of Manufacturing Science and Technology* 33 (2021) 389–397.
- [17] H.F. Al-Harbi, M. Knezevic, S.R. Kalidindi, Spectral approaches for the fast computation of yield surfaces and first-order plastic property closures for polycrystalline materials with cubic-triclinic textures, *Comput. Mater. Continua (CMC): Comput. Mater. Continua (CMC)* 15 (2010) 153–172.
- [18] R. Xiong, H. Peng, H. Si, W. Zhang, Y. Wen, Thermodynamic calculation of stacking fault energy of the Fe–Mn–Si–C high manganese steels, *Mater. Sci. Eng.* 598 (2014) 376–386.
- [19] E. Galindo-Nava, P. Rivera-Díaz-del-Castillo, Understanding martensite and twin formation in austenitic steels: a model describing TRIP and TWIP effects, *Acta Mater.* 128 (2017) 120–134.
- [20] S.S. Nene, M. Frank, K. Liu, R.S. Mishra, B.A. McWilliams, K.C. Cho, Extremely high strength and work hardening ability in a metastable high entropy alloy, *Sci. Rep.* 8 (2018) 9920.
- [21] R. Xiong, H. Peng, S. Wang, H. Si, Y. Wen, Effect of stacking fault energy on work hardening behaviors in Fe–Mn–Si–C high manganese steels by varying silicon and carbon contents, *Mater. Des.* 85 (2015) 707–714.
- [22] J.J. Jonas, C. Aranas Jr., S.F. Rodriguez, Dynamical Transformation of Austenite at Temperatures above the Ae_3 , *Materials Science Forum*, Trans Tech Publ, 2018, pp. 633–638.
- [23] S.S. Nene, K. Liu, M. Frank, R.S. Mishra, R.E. Brennan, K.C. Cho, Z. Li, D. Raabe, Enhanced strength and ductility in a friction stir processing engineered dual phase high entropy alloy, *Sci. Rep.* 7 (2017) 1–7.
- [24] S. Bhowmik, J. Zhang, S.C. Vogel, S.S. Nene, R.S. Mishra, B.A. McWilliams, M. Knezevic, Effects of plasticity-induced martensitic transformation and grain refinement on the evolution of microstructure and mechanical properties of a metastable high entropy alloy, *J. Alloys Compd.* 891 (2022), 161871.
- [25] J. Weiss, E. Vasilev, M. Knezevic, Assessing Strength of Phases in a Quadruplex High Entropy Alloy via High-Throughput Nanoindentation to Clarify Origins of Strain Hardening Mater. Charact., 2023.
- [26] N. Stepanov, D. Shaysultanov, G. Salishchev, M. Tikhonovsky, E. Oleynik, A. Tortika, O. Senkov, Effect of V content on microstructure and mechanical properties of the CoCrFeMnNiVx high entropy alloys, *J. Alloys Compd.* 628 (2015) 170–185.
- [27] A. Heczel, M. Kawasaki, J.L. Lábár, J.-i. Jang, T.G. Langdon, J. Gubicza, Defect structure and hardness in nanocrystalline CoCrFeMnNi high-entropy alloy processed by high-pressure torsion, *J. Alloys Compd.* 711 (2017) 143–154.
- [28] V.H. Hammond, M.A. Atwater, K.A. Darling, H.Q. Nguyen, L.J. Kecske, Equal-channel angular extrusion of a low-density high-entropy alloy produced by high-energy cryogenic mechanical alloying, *Jom* 66 (2014) 2021–2029.
- [29] M. Jahedi, M. Knezevic, M. Paydar, High-pressure double torsion as a severe plastic deformation process: experimental procedure and finite element modeling, *J. Mater. Eng. Perform.* 24 (2015) 1471–1482.
- [30] M. Jahedi, M.H. Paydar, S. Zheng, I.J. Beyerlein, M. Knezevic, Texture evolution and enhanced grain refinement under high-pressure-double-torsion, *Mater. Sci. Eng.* 611 (2014) 29–36.
- [31] S. Palanivel, A. Arora, K. Doherty, R. Mishra, A framework for shear driven dissolution of thermally stable particles during friction stir welding and processing, *Mater. Sci. Eng.* 678 (2016) 308–314.
- [32] R.Z. Valiev, T.G. Langdon, Principles of equal-channel angular pressing as a processing tool for grain refinement, *Prog. Mater. Sci.* 51 (2006) 881–981.
- [33] A.P. Zhilyaev, T.G. Langdon, Using high-pressure torsion for metal processing: fundamentals and applications, *Prog. Mater. Sci.* 53 (2008) 893–979.
- [34] S.S. Nene, M. Frank, K. Liu, S. Sinha, R.S. Mishra, B.A. McWilliams, K.C. Cho, Corrosion-resistant high entropy alloy with high strength and ductility, *Scripta Mater.* 166 (2019) 168–172.
- [35] K. Liu, S.S. Nene, M. Frank, S. Sinha, R.S. Mishra, Extremely high fatigue resistance in an ultrafine grained high entropy alloy, *Appl. Mater. Today* 15 (2019) 525–530.
- [36] P. Agrawal, S. Shukla, S. Gupta, P. Agrawal, R.S. Mishra, Friction stir gradient alloying: a high-throughput method to explore the influence of V in enabling HCP to BCC transformation in a γ -FCC dominated high entropy alloy, *Appl. Mater. Today* 21 (2020), 100853.
- [37] D.H. Smith, J. Bicknell, L. Jorgensen, B.M. Patterson, N.L. Cordes, I. Tsukrov, M. Knezevic, Microstructure and mechanical behavior of direct metal laser sintered Inconel alloy 718, *Mater. Char.* 113 (2016) 1–9.
- [38] S.R. Kalidindi, A. Abusafieh, E. ElDanaf, Accurate characterization of machine compliance for simple compression testing, *Exp. Mech.* 37 (1997) 210–215.
- [39] L. Lutterotti, M. Bortolotti, G. Ischia, I. Lonardelli, H.-R. Wenk, Rietveld texture analysis from diffraction images, in: K. Deutsche Gesellschaft für (Ed.), *Tenth European Powder Diffraction Conference*, Oldenbourg Wissenschaftsverlag, 2007, pp. 125–130. München.
- [40] H.-R. Wenk, L. Lutterotti, S. Vogel, Rietveld texture analysis from TOF neutron diffraction data, *Powder Diffr.* 25 (2010) 283–296.
- [41] N.C. Ferreri, R. Pokharel, V. Livescu, D.W. Brown, M. Knezevic, J.-S. Park, M. A. Torrez, G.T. Gray, Effects of heat treatment and build orientation on the evolution of ϵ and α' martensite and strength during compressive loading of additively manufactured 304L stainless steel, *Acta Mater.* 195 (2020) 59–70.
- [42] D.J. Savage, L. Lutterotti, C.M. Biwer, M. McKerns, C. Bolme, M. Knezevic, S. C. Vogel, MILK: a Python scripting interface to MAUD for automation of Rietveld analysis, *J. Appl. Crystallogr.* 56 (2023).
- [43] F. Bachmann, R. Hielscher, H. Schaeber, Texture analysis with MTEX – free and open source software toolbox, *Solid State Phenom.* 160 (2010) 63–68.
- [44] L. Bracke, L. Kestens, J. Penning, Transformation mechanism of α' -martensite in an austenitic Fe–Mn–C–N alloy, *Scripta Mater.* 57 (2007) 385–388.
- [45] M. Zecevic, R.J. McCabe, M. Knezevic, Spectral database solutions to elasto-viscoplasticity within finite elements: application to a cobalt-based FCC superalloy, *Int. J. Plast.* 70 (2015) 151–165.
- [46] Z. Feng, R. Pokharel, S.C. Vogel, R.A. Lebensohn, D. Pagan, E. Zepeda-Alarcon, B. Clausen, R. Martinez, G.T. Gray, M. Knezevic, Crystal plasticity modeling of strain-induced martensitic transformations to predict strain rate and temperature sensitive behavior of 304 L steels: applications to tension, compression, torsion, and impact, *Int. J. Plast.* 156 (2022), 103367.
- [47] M. Zecevic, I.J. Beyerlein, M. Knezevic, Activity of pyramidal I and II $<\text{c+a}>$ slip in Mg alloys as revealed by texture development, *J. Mech. Phys. Solid.* 111 (2018) 290–307.
- [48] S. Nene, M. Frank, P. Agrawal, S. Sinha, K. Liu, S. Shukla, R. Mishra, B. McWilliams, K. Cho, Microstructurally flexible high entropy alloys: linkages between alloy design and deformation behavior, *Mater. Des.* 194 (2020), 108968.
- [49] G.B. Olson, M. Cohen, A mechanism for the strain-induced nucleation of martensitic transformations, *Journal of the Less Common Metals* 28 (1972) 107–118.
- [50] G.B. Olson, M. Cohen, Kinetics of strain-induced martensitic nucleation, *MTA* 6 (1975) 791.
- [51] G.B. Olson, M. Cohen, A general mechanism of martensitic nucleation: Part I. General concepts and the FCC–HCP transformation, *MTA* 7 (1976) 1897–1904.
- [52] Z. Feng, M. Zecevic, M. Knezevic, Stress-assisted ($\gamma \rightarrow \alpha'$) and strain-induced ($\gamma \rightarrow \epsilon \rightarrow \alpha'$) phase transformation kinetics laws implemented in a crystal plasticity model for predicting strain path sensitive deformation of austenitic steels, *Int. J. Plast.* 136 (2021), 102807.
- [53] W.G. Burgers, J.A. Klostermann, Influence of the direction of deformation on the transition of austenite into martensite, *Acta Metall.* 13 (1965) 568–572.
- [54] D. Goodchild, W.T. Roberts, D.V. Wilson, Plastic deformation and phase transformation in textured austenitic stainless steel, *Acta Metall.* 18 (1970) 1137–1145.
- [55] B. Petit, N. Gey, M. Cherkaoui, B. Bolle, M. Humbert, Deformation behavior and microstructure/texture evolution of an annealed 304 AISI stainless steel sheet. Experimental and micromechanical modeling, *Int. J. Plast.* 23 (2007) 323–341.
- [56] E. Polatidis, W.N. Hsu, M. Šmid, T. Panzner, S. Chakrabarty, P. Pant, H. Van Swygenhoven, Suppressed martensitic transformation under biaxial loading in low stacking fault energy metastable austenitic steels, *Scripta Mater.* 147 (2018) 27–32.
- [57] M. Zecevic, M.V. Upadhyay, E. Polatidis, T. Panzner, H. Van Swygenhoven, M. Knezevic, A crystallographic extension to the Olson-Cohen model for predicting

- strain path dependence of martensitic transformation, *Acta Mater.* 166 (2019) 386–401.
- [58] R. Lagneborg, The martensite transformation in 18% Cr-8% Ni steels, *Acta Metall.* 12 (1964) 823–843.
- [59] R.S. Mishra, S. Gupta, Microstructural engineering through high enthalpy states: implications for far-from-equilibrium processing of structural alloys, *Frontiers in Metals and Alloys* 2 (2023), 1135481.
- [60] Y. Bu, Z. Li, J. Liu, H. Wang, D. Raabe, W. Yang, Nonbasal slip systems enable a strong and ductile hexagonal-close-packed high-entropy phase, *Phys. Rev. Lett.* 122 (2019), 075502.
- [61] U.F. Kocks, C.N. Tomé, H.-R. Wenk, *Texture and Anisotropy*, Cambridge University Press, Cambridge, UK, 1998.
- [62] M. Knezevic, I.J. Beyerlein, Multiscale modeling of microstructure-property relationships of polycrystalline metals during thermo-mechanical deformation, *Adv. Eng. Mater.* 20 (2018), 1700956.
- [63] M. Zecevic, I.J. Beyerlein, M. Knezevic, Coupling elasto-plastic self-consistent crystal plasticity and implicit finite elements: applications to compression, cyclic tension-compression, and bending to large strains, *Int. J. Plast.* 93 (2017) 187–211.
- [64] M. Wang, Z. Li, D. Raabe, In-situ SEM observation of phase transformation and twinning mechanisms in an interstitial high-entropy alloy, *Acta Mater.* 147 (2018) 236–246.
- [65] M. Frank, Y. Chen, S.S. Nene, S. Sinha, K. Liu, K. An, R.S. Mishra, Investigating the deformation mechanisms of a highly metastable high entropy alloy using in-situ neutron diffraction, *Mater. Today Commun.* 23 (2020), 100858.
- [66] R.S. Mishra, S.S. Nene, M. Frank, S. Sinha, K. Liu, S. Shukla, Metastability driven hierarchical microstructural engineering: overview of mechanical properties of metastable complex concentrated alloys, *J. Alloys Compd.* 842 (2020), 155625.